

Nonlinear Methods for Shape Optimization Problems in Liquid Crystal Tactoids

J. H. Adler^a, A. S. Andrei^{a,*}, T. J. Atherton^b

^a*Department of Mathematics, Tufts University, Medford, MA 02155*

^b*Department of Physics and Astronomy, Tufts University, Medford, MA 02155*

Abstract

Anisotropic fluids, such as nematic liquid crystals, can form non-spherical equilibrium shapes known as tactoids. Predicting the shape of these structures as a function of material parameters is challenging and paradigmatic of a broader class of problems that combine shape and order. Here, we develop a discrete shape optimization approach with finite elements to find the configuration of a two-dimensional tactoid using the Landau de Gennes framework and a Q-tensor representation. Efficient solution of the resulting constrained energy minimization problem is achieved using a quasi-Newton and nested iteration algorithm. Numerical validation is performed with benchmark solutions and compared against experimental data and earlier work. We explore physically motivated subproblems, whereby the shape and order are separately held fixed, to explore the role of both and examine material parameter dependence of the convergence. Nested iteration significantly improves both the computational cost and convergence of numerical solutions of these highly deformable materials.

Keywords: Tactoids; shape optimization; quasi-Newton's method; gradient descent methods; nested iteration, nematic liquid crystals

1. Introduction

Liquid crystals (LCs) are intermediate states of matter that exhibit long-range order like a crystal but retain fluid properties [1]. The *nematic* LC phase, in particular, lacks translational order but possesses orientational order characterized by a locally-preferred axis of molecular or particulate alignment; this direction may vary spatially at the cost of elastic energy. Due to the presence of orientational order, nematic liquid crystals have anisotropic properties, such as surface tension, dielectric response and elasticity. In contrast to an isotropic fluid, which only exhibits surface tension and no elastic effects, LCs may form non-spherical droplets known as *tactoids* [2] when suspended in a surrounding host isotropic fluid. Tactoids can assume various shapes and director field configurations depending on their size [2], elastic properties, and anisotropic surface tension strength

*Corresponding author

Email addresses: James.Adler@tufts.edu (J. H. Adler), Anca.Andrei@tufts.edu (A. S. Andrei), Timothy.Atherton@tufts.edu (T. J. Atherton)

Preprint submitted to Computational Physics

October 9, 2023

[3]. Due to their potential to change shape and ability to conform to complex geometries [4, 5], tactoids are an exciting material for emerging technologies [6]. This includes enhancing LC displays’ performance [7], serving as carriers for pharmaceuticals [8, 9], and developing materials with adaptive stiffness as seen in soft robots [10, 11, 12].

In this paper, we develop efficient and robust numerical methods based on nonlinear optimization techniques to predict the solution to tactoid shape-order problems. Using this approach, we compare our results with earlier work, Bates [13] and Prinsen and van der Schoot [2], all while improving upon previous research on modeling tactoids’ various morphologies.

Numerical efforts to investigate the configuration of a nematic tactoid droplet have received extensive attention. Monte Carlo simulations have shown that a tactoid’s aspect ratio can be temperature dependent [14] and that their morphologies can depend on the LC’s orientational ordering [15]. For instance, various tactoid formations are determined by competition between the bending and surface tension energies as LCs exhibit phase transitions [16]. Monte Carlo methods have also been used to model tactoid defects [4, 17, 5]. While Monte Carlo methods are versatile, they are computationally expensive and require many simplifying assumptions on the model to achieve convergence. Phase field methods use an auxiliary scalar field to interpolate between the interior and exterior of a shape and have been used for modeling tactoids [17]. Such methods are powerful, but challenges arise when dealing with cusps in the manifold [18]. Level set methods, which represent the free boundary of the system as a contour or a level set of a scalar function defined in a higher-dimensional space, have been used to model interfaces of tactoids and depict their defects [19]. While level set methods can model materials that change shape and topology, they require sophisticated numerical techniques, and including constraints can be challenging [20].

In contrast, finite-element discretizations with gradient descent (GD) based algorithms have been designed to iteratively adjust the position and orientational degrees of freedom in the tactoid to find stable nematic tactoid solutions under different conditions [21, 22]. DeBenedictis *et al.* [23] use a director formulation and Frank-Oseen energy to develop an alternating optimization scheme that takes GD iterations to solve for the director configuration, then solves for the optimal shape and repeats until convergence. While GD methods are computationally cheap with gradient-only calculations and are easy to implement, they possess linear convergence and hence need a high number of iterations to converge.

This paper aims to improve upon [23] by developing an integrated optimization method that simultaneously determines the shape and director configuration while ensuring physical validity. Predicting the optimal shape and physical fields involves solving a nonlinearly constrained optimization problem where we minimize the sum of bulk terms defined on a manifold, \mathcal{M} , and surface terms defined on the boundary $\partial\mathcal{M}$ while satisfying a nonlinear volumetric or surface area constraint. To expedite convergence, we use Newton’s method with Lagrange multiplier theory [24, 25], which offers local quadratic convergence and fewer iterations for faster solutions. However, Newton’s method demands the Hessian matrix of all functionals concerning shape and field and is sensitive to initial guesses, potentially hindering convergence to the correct solution. To mitigate computational expense, we approximate the Hessian using the well-established BFGS quasi-Newton method, sacrificing quadratic for local superlinear convergence. The method is implemented and run for physically relevant parameters, reproducing several

expected physical phenomena. We use nested iteration and Newton damping with line search [26, 25] to handle relatively inaccurate initial guesses for efficient iterative convergence. Nested iteration techniques are a hierarchical approach to solving complex numerical problems, where coarse-grid solutions are used to accelerate convergence on finer grids, improving computational efficiency [27, 28, 29]. Nested iteration has been successfully applied to a variety of problems, including LC optimization problems [30]. Here, we demonstrate its efficiency in resolving the above-mentioned tactoid shapes.

Finally, we note that a great amount of work has been done on solution methods for solving LC problems in fixed boundaries. This includes deflation and parameter continuation for finding multiple stable LC configurations [31, 32, 33, 34] and multigrid preconditioners for the resulting linear systems [35, 36, 37, 38] to improve performance. As our focus is on the nonlinear methods with nested iteration, we use direct solvers when needed and consider multigrid methods as future work.

The remainder of the paper is organized as follows. We first pose the shape optimization problem and construct its discrete version in Section 2. In Section 3, we derive the GD method from [23], the all-in-one quasi-Newton-based method, and describe the nested iteration approach used to improve computational efficiency in finding the optimal nematic tactoid shape. Numerical experiments are reported in Section 4. Together with the full problem, we study two physically motivated subproblems, whereby either the shape or liquid crystal itself is held fixed, to understand the role of each better. We give concluding remarks in Section 5 and consider opportunities for future work.

2. Q-tensor Model for Tactoids

The configuration of a nematic liquid crystal is described by a vector or tensor field that encodes information about the local orientational ordering. Several choices of representation are commonly used. The first possibility is to represent the local average molecular orientation by a unit vector field known as the *director*, \mathbf{n} . The director fully describes the nematic in the absence of *disclinations*, special points where \mathbf{n} is not uniquely defined and $\nabla \mathbf{n}$ diverges. If the director formulation is used, \mathbf{n} is a minimizer of the Frank-Oseen free energy model [39, 24] subject to the constraint that $\mathbf{n} \cdot \mathbf{n} = 1$ everywhere.

An alternative formulation, known as the Q-tensor approach [40, 1], encodes both orientational information as well as the local degree of alignment, denoted by a scalar field S , into a single tensor order parameter. In three dimensions, and assuming that the alignment is uniaxial, the Q-tensor has the form,

$$\mathcal{Q} = S \left(\mathbf{n} \otimes \mathbf{n} - \frac{\mathcal{I}}{3} \right), \quad (1)$$

where \mathcal{I} is the identity matrix and, again, S is the scalar order parameter. By construction, \mathcal{Q} is symmetric and traceless, and both properties can be enforced by parameterization. In the isotropic phase, where there is no orientational order, $\mathcal{Q} = 0$, i.e., a zero-tensor. Given an instance of \mathcal{Q} , both \mathbf{n} and S can be reconstructed by eigenanalysis: the largest eigenvalue of \mathcal{Q} is $\frac{2}{3}S$ and \mathbf{n} is the associated normalized eigenvector. The Q-tensor approach has a number of advantages over the director formulation. For one, it permits defects since when large gradients of \mathbf{n} arise, S compensates by tending to zero;

it can accommodate defects with a non-integer winding number naturally. Moreover, it obviates the need to impose any length constraints. Generally, these advantages are at the expense of requiring more degrees of freedom overall.

The local values of \mathcal{Q} are obtained by minimizing a free energy that includes bulk terms defined on a manifold, \mathcal{M} , and surface terms defined on the boundary $\partial\mathcal{M}$. The free energy has the form,

$$\mathcal{F}(\mathbf{x}, \mathcal{Q}, \nabla \mathcal{Q}, \dots) = \int_{\mathcal{M}} f(\mathbf{x}, \mathcal{Q}, \nabla \mathcal{Q}, \dots) d\mathbf{x} + \int_{\partial\mathcal{M}} g(\mathbf{x}, \mathcal{Q}, \nabla \mathcal{Q}, \dots) ds, \quad (2)$$

where $\mathbf{x} \in \mathcal{M}$ and f and g are linear or nonlinear energy densities that depend on \mathcal{Q} and its derivatives. The function g is defined on $\partial\mathcal{M}$ and may impose a preferred orientation of the LC relative to the boundary tangent plane or normal vector, a phenomenon referred to as *anchoring*. Furthermore, the minimization may be subject to nonlinear *global* (integral) equality constraints that can be used to fix the manifold's volume,

$$\mathcal{C}(\mathcal{Q}, \nabla \mathcal{Q}) = \int_{\mathcal{M}} c(\mathcal{Q}, \nabla \mathcal{Q}) d\mathbf{x} = 0. \quad (3)$$

In this work, we adopt a particular choice of free energy sufficient to capture the physics of nematic tactoids,

$$\begin{aligned} \mathcal{F}(\mathbf{x}, \mathcal{Q}, \nabla \mathcal{Q}) = & \int_{\mathcal{M}} a \operatorname{tr}(\mathcal{Q}^2) + \frac{2b}{3} \operatorname{tr}(\mathcal{Q}^3) + \frac{c}{2} \operatorname{tr}(\mathcal{Q}^2)^2 + \frac{L_1}{2} |\nabla \mathcal{Q}|^2 d\mathbf{x} \\ & + \int_{\partial\mathcal{M}} \sigma + \frac{W}{2} \operatorname{tr}(\mathcal{Q} - \mathcal{Q}_s)^2 ds, \end{aligned} \quad (4)$$

where the first three bulk terms represent a Landau expansion of the free energy of \mathcal{Q} with Landau coefficients a , b , and c . These parameters, in effect, select a particular uniform value of S in the bulk; by convention, a is chosen to be temperature dependent, $a = a_0(T - T_0)$, where T_0 is the temperature below which the isotropic phase is no longer stable. The fourth term in $\nabla \mathcal{Q}$ represents elasticity, and here, we adopt the commonly used one-constant approximation with a single elastic constant L_1 . On the boundary, $\partial\mathcal{M}$, the constant term with prefactor σ represents the isotropic surface tension. The second term is the anisotropic surface tension with anchoring coefficient W and is constructed to favor the alignment of the LC in the tangent plane of the boundary surface. The preferred surface values of tensor \mathcal{Q}_s are constructed from the local tangent vector \mathbf{t} ,

$$\mathcal{Q}_s = S_0 \left(\mathbf{t} \otimes \mathbf{t} - \frac{\mathcal{I}}{3} \right), \quad (5)$$

where S_0 is the degree of order induced by the surface, which may differ from the value set by the Landau coefficients in the bulk depending on the chemistry of the liquid crystal-host interface. Additionally, since we consider two-dimensional examples in this paper, the global equality constraint preserves area, maintaining the stability of tactoids of varying sizes at coexistence:

$$\mathcal{C}(\mathbf{x}) = \int_{\mathcal{M}} d\mathbf{x} - A_0 = 0. \quad (6)$$

Here, A_0 is the target area of the tactoid.

In this paper, we model two-dimensional tactoids where \mathbf{n} lies parallel to the plane of the tactoid. Hence, \mathcal{Q} can be described by a reduced parameterization that may be displayed in matrix form,

$$\mathcal{Q} = \begin{bmatrix} q_{xx} & q_{xy} & 0 \\ q_{xy} & \frac{1}{3} - q_{xx} & 0 \\ 0 & 0 & -\frac{1}{3} \end{bmatrix}, \quad (7)$$

and includes only two independent degrees of freedom q_{xx} and q_{xy} . We nondimensionalize \mathcal{F} and \mathcal{C} by introducing a length scale ξ , so that $\mathbf{x} \rightarrow \xi \bar{\mathbf{x}}$, and divide (4) by L_1 to get,

$$\begin{aligned} \bar{\mathcal{F}}(\bar{\mathbf{x}}, \mathcal{Q}) &= \int_{\mathcal{M}} \bar{a} \operatorname{tr}(\mathcal{Q}^2) + \frac{2\bar{b}}{3} \operatorname{tr}(\mathcal{Q}^3) + \frac{\bar{c}}{2} \operatorname{tr}(\mathcal{Q}^2)^2 + \frac{1}{2} |\nabla \mathcal{Q}|^2 d\bar{\mathbf{x}} \\ &\quad + \bar{\tau} \int_{\partial \mathcal{M}} 1 + \frac{\bar{\omega}}{2} \operatorname{tr}(\mathcal{Q} - \mathcal{Q}_s)^2 ds, \end{aligned} \quad (8)$$

with dimensionless parameters,

$$\bar{a} = \frac{a\xi^2}{L_1}, \quad \bar{b} = \frac{b\xi^2}{L_1}, \quad \bar{c} = \frac{c\xi^2}{L_1}, \quad \bar{\tau} = \frac{\sigma\xi}{L_1}, \quad \bar{\omega} = \frac{W}{\sigma}. \quad (9)$$

The constraint, (6), remains unchanged as A_0 is assumed to be dimensionless. Hence, to find the equilibrium order and spatial coordinates, we minimize (8) subject to the global constraint (6). For the rest of the paper, we assume all quantities are suitably nondimensionalized and drop the bar notation.

To set up the discrete optimization problem, we represent \mathcal{M} as a simplicial complex denoted by M consisting of p spatial coordinate points, $\mathbf{x}_i \in M$, $1 \leq i \leq p$. Using linear finite elements, we discretize the Q-tensor, (7), over M with degrees of freedom defined as $Q_i := \mathcal{Q}(\mathbf{x}_i)$ at each point $\mathbf{x}_i \in M$. Note that this corresponds to two degrees of freedom for q_{xx} and q_{xy} at each vertex. Other finite-element approaches for Q-tensor models have been considered in [38, 41, 42], as well as for other LC frameworks [43, 44, 45].

Then, $\mathcal{F}(\mathbf{x}, \mathcal{Q})$ and $\mathcal{C}(\mathbf{x})$ are defined over M to obtain $F(\mathbf{x}, Q)$ and $C(\mathbf{x})$,

$$\begin{aligned} F(\mathbf{x}, Q) &= \int_M a \operatorname{tr}(Q^2) + \frac{2b}{3} \operatorname{tr}(Q^3) + \frac{c}{2} \operatorname{tr}(Q^2)^2 + \frac{1}{2} |\nabla Q|^2 d\mathbf{x} \\ &\quad + \tau \int_{\partial M} 1 + \frac{\omega}{2} \operatorname{tr}(Q - Q_s)^2 ds, \end{aligned} \quad (10)$$

$$C(\mathbf{x}) = \sum_{i=1}^{p-2} \frac{1}{2} \|(\mathbf{x}_{i+1} - \mathbf{x}_i) \times (\mathbf{x}_{i+2} - \mathbf{x}_{i+1})\|, \quad (11)$$

where $\mathbf{x} \in M$ and Q is the set of degrees of freedom of the Q-tensor defined on M . Note that (11) is the sum of the area of each element in the simplicial complex. The corresponding discrete shape optimization problem is then defined as,

$$\begin{aligned} (M^*, Q^*) &= \arg \min_{\mathbf{x} \in M, Q} F(\mathbf{x}, Q), \\ \text{s.t. } 0 &= C(\mathbf{x}). \end{aligned} \quad (12)$$

Here, M^* and Q^* represent the equilibrium configurations of the manifold and the Q-tensor values at each point in M for the minimized configuration.

3. Energy Minimization of the Discrete Tactoid Energy

With the discrete (\mathbf{x}, Q) shape optimization problem (12) just derived, we now describe both the GD-based and Newton-based methods considered. We note that the GD-based method in [23] was formulated for a director formulation with a Frank-Oseen energy [39]; we, therefore, describe in the first subsection how the method is modified for the Q-tensor formulation used in this paper. Next, we discuss the quasi-Newton approach, which is the main target of this work, and nested iteration, which is used to improve the performance of both methods.

3.1. Gradient Descent

To start, we describe the gradient descent algorithm used in [23] modified for the Q-tensor framework. The authors noted that the combined (\mathbf{x}, \mathbf{n}) optimization problem exhibited stiffness due to intrinsic differences in length scale between the vertex, \mathbf{x} , and director, \mathbf{n} , degrees of freedom. To alleviate this, they used an alternating gradient descent scheme, first taking descent steps in \mathbf{n} followed by \mathbf{x} and repeating until convergence. Given a similar connection between \mathbf{x} and Q , we use a similar approach.

Consider a vector of the spatial vertices at the k^{th} iteration, $\mathbf{x}^k \in M^k$, where M^k is the current triangulation of the grid, M . We first compute the gradients of F and C with respect to \mathbf{x} on the given grid M , denoted by F_M^k , and C_M^k , respectively, and evaluate each at $\mathbf{x}_i \in M^k$ so both are column vectors of size $2p$. This trio of current data, $\{\mathbf{x}^k, F_M^k, C_M^k\}$ is then projected onto the constraint's tangent space,

$$\tilde{\mathbf{x}}^k \leftarrow \mathbf{x}^k + \alpha_k \left(F_M^k - \frac{F_M^k \cdot C_M^k}{C_M^k \cdot C_M^k} C_M^k \right). \quad (13)$$

Note that α_k is the k^{th} -iteration step-size found from performing a one-dimensional line search. The update defined in (13) is an intermediate step towards finding $\mathbf{x}^{k+1} \in M^{k+1}$ since $\tilde{\mathbf{x}}^k$ only satisfies the constraint to linear order. Following [23], we perform additional reprojection steps,

$$\tilde{\mathbf{x}}^k \leftarrow \tilde{\mathbf{x}}^k + \frac{C(\tilde{\mathbf{x}}^k)}{C_M^k \cdot C_M^k} C_M^k. \quad (14)$$

In each reprojection step, C_M^k is evaluated at $\tilde{\mathbf{x}}_i \in \tilde{M}^k$. The prefactor, $\frac{C(\tilde{\mathbf{x}}^k)}{C_M^k \cdot C_M^k}$, represents the difference between the constraint value and its target; reprojection steps are repeated until the constraint is satisfied to a given tolerance. This projected value is used as the next iterate $\mathbf{x}^{k+1} \leftarrow \tilde{\mathbf{x}}^k$.

To find Q we follow a similar procedure but with $\{Q^k, F_Q^k\}$,

$$Q^{k+1} \leftarrow Q^k + \beta_k F_Q^k, \quad (15)$$

where β_k is obtained with a separate one-dimensional line search. A second projection is unnecessary as the global constraint only depends on $\mathbf{x} \in M$. In practice, [23] starts by optimizing for the field and then for the spatial coordinates.

3.2. Quasi-Newton

The GD algorithm introduced in the previous section converges quite slowly and can stagnate under certain conditions. It also incorporates a number of metaparameters, such as the number of alternating iterations to be taken for shape and field degrees of freedom that must be hand-tuned for each problem. To address these issues, we develop a quasi-Newton (QN) based method to solve the full (\mathbf{x}, Q) minimization problem all at once. Given the presence of the nonlinear constraint, we introduce the Lagrangian \mathcal{L} of the system based on (12),

$$\mathcal{L}(\mathbf{x}, Q, \lambda) = F(\mathbf{x}, Q) - \lambda C(\mathbf{x}), \quad (16)$$

where $\lambda \in \mathbb{R}$. The necessary first-order optimality conditions are

$$\mathcal{L}_M := F_M - \lambda C_M = \mathbf{0}, \quad (17)$$

$$\mathcal{L}_Q := F_Q = \mathbf{0}, \quad (18)$$

$$\mathcal{L}_\lambda := -C(\mathbf{x}) = 0, \quad (19)$$

where F_M and F_Q are the first-order Gateaux derivatives with respect to every $\mathbf{x}_i \in M$ and Q_i on M , respectively (i.e., the gradients as computed for GD). Given that there are two degrees of freedom per \mathbf{x} and Q in two dimensions, both \mathcal{L}_M and \mathcal{L}_Q are column vectors of size $2p$, and \mathcal{L}_λ is a scalar.

These equations are nonlinear, so we linearize (17)-(19) and set up the corresponding iterative scheme. Let $(\mathbf{x}^k, Q^k, \lambda^k)$ be the current approximations for (\mathbf{x}, Q, λ) , respectively. The update, $(\mathbf{d}_M, \mathbf{d}_Q, d_\lambda)$, to the approximation is the solution to the QN iteration,

$$\begin{bmatrix} \mathbf{d}_{M,Q} \\ d_\lambda \end{bmatrix} = \begin{bmatrix} \mathbf{B}^k & -(\mathbf{A}^k)^T \\ -\mathbf{A}^k & 0 \end{bmatrix}^{-1} \begin{bmatrix} \mathbf{R}^k \\ -\mathcal{L}_\lambda \end{bmatrix} =: \mathcal{A}^{-1} \mathcal{R}, \quad (20)$$

with

$$\mathbf{d}_{M,Q} = \begin{bmatrix} \mathbf{d}_M \\ \mathbf{d}_Q \end{bmatrix}, \quad \mathbf{A}^k = \begin{bmatrix} C_M & \mathbf{0} \end{bmatrix}, \quad \mathbf{R}^k = \begin{bmatrix} -\mathcal{L}_M \\ -\mathcal{L}_Q \end{bmatrix}.$$

Here, \mathbf{B}^k is an approximation to the Hessian of the (\mathbf{x}, Q) portion of the Lagrangian, \mathbf{A}^k contains the gradient of the constraint function at \mathbf{x}^k , and \mathbf{R}^k is the nonlinear residual for the (\mathbf{x}, Q) portion of the system. Since \mathcal{A} is a saddle-point matrix, which poses challenges for building efficient solvers, we choose a BFGS approximation and use explicit formulae to compute $(\mathbf{B}^k)^{-1}$ and \mathcal{A}^{-1} [46].

Next, we find the step size for the field, α_Q , and the step size for the spatial coordinates α_M . The step size α_Q is found with backtracking line search such that it satisfies,

$$F(\mathbf{x}^k, Q^k + \alpha_Q \mathbf{d}_Q) \leq F(\mathbf{x}^k, Q^k) + \eta \alpha_Q (F_Q^k)^T \mathbf{d}_Q, \quad (21)$$

where $\eta \in (0, 1)$. Then, we update the field accordingly,

$$Q^{k+1} \leftarrow Q^k + \alpha_Q \mathbf{d}_Q. \quad (22)$$

The step size α_M for the spatial coordinates is found using an ℓ^1 monitor function [47] defined as

$$\phi(\mathbf{x}, Q^k, \mu) := F(\mathbf{x}, Q^k) + \mu \|C(\mathbf{x})\|_1, \quad (23)$$

where $\mu \in \mathbb{R}$ is a penalty term for the constraint. This monitor function decides what factor of \mathbf{d}_M and d_λ should be accepted in order to decrease $F(\mathbf{x}^{k+1}, Q^k)$. Similar to finding α_Q , we use backtracking until the following inequality is satisfied,

$$\phi(\mathbf{x}^k + \alpha_M \mathbf{d}_M, Q^k, \mu_k) \leq \phi(M^k, Q^k, \mu_k) + \eta \alpha_M (\phi_M^k)^T \mathbf{d}_M,$$

where $\eta \in (0, 1)$, $\mu_k = \|\lambda_k\|_\infty$, and

$$(\phi_M^k)^T \mathbf{d}_M := \alpha_M F_M^k \mathbf{d}_M - \mu_k \|C(\mathbf{x}^k)\|_1. \quad (24)$$

Finally, we update the spatial coordinates and Lagrange multiplier,

$$\mathbf{x}^{k+1} \leftarrow \mathbf{x}^k + \alpha_M \mathbf{d}_M \quad (25)$$

$$\lambda^{k+1} \leftarrow \lambda^k + \alpha_M d_\lambda. \quad (26)$$

3.3. Nested Iteration

Both QN and GD, as described above, are sensitive to initial guesses. In particular, as the anisotropic surface tension parameters increase, we expect to see the nematic LC tactoids elongating towards the characteristic eye shape [14, 2]. Numerically, this means that by starting from the same initial guess for every parameter value, we may not be close to the basin of attraction for some regions of parameter space. This can lead the method to stagnate at locally optimal solutions, not the expected global minima. To remedy this issue, we wrap each method with nested iteration.

Nested iteration [27, 28] begins with an initial coarse grid, denoted by M_i with only a few vertex points, p , that represents the problem domain. This coarse grid may not capture all the details of the solution, but solving the nonlinear system on this grid is computationally inexpensive. Thus, (12) is solved on the coarse grid with either QN or GD until a preferred convergence criterion is reached. The coarse grid, M_i , is then subdivided into smaller elements. In this work, we consider uniform refinement such that each element is divided into four smaller but similar elements of equal size. The coarse solution from M_i is then linearly interpolated onto the finer grid M_{i+1} and used as an initial guess for solving the problem now represented on M_{i+1} of size $4p$ (in two-dimensions). This initial solution on M_{i+1} should then be a more accurate guess as it came from solving a similar problem on M_i , and thus fewer iterations to converge are expected.

4. Numerical Results

We demonstrate the robustness of QN combined with Nested Iteration (NI) on a challenging two-dimensional problem involving the formation of a nematic tactoid. We compare the approach with the GD-based techniques described in Section 3.1. Numerical methods and benchmark tests are implemented and executed in *Morpho*, an open-source

programmable environment for shape optimization [48]. *Morpho* is able to evaluate the objective function of interest as well as its gradients with respect to the configuration's and field's degrees of freedom. Furthermore, grid quality control in *Morpho* does not require user intervention and provides the user the option of automatic domain refinement and easy object-oriented programming. All timed numerical results are done using a workstation with an 8-core 3-GHz Intel Xeon Sandy Bridge CPU and 256 GB of RAM.

We use material constants from [40] with $a_0 = 0.042 \times 10^6 \text{ Nm}^{-2} \text{K}^{-1}$ and $T - T_0 = -0.1 \text{ K}$. Thus, the prefactors in (8) are:

$$a = -0.042 \times 10^5 \text{ Nm}^{-2}, \quad b = -0.64 \times 10^6 \text{ Nm}^{-2}, \quad (27)$$

$$c = 0.35 \times 10^6 \text{ Nm}^{-2}, \quad L_1 = 1 \times 10^{-11} \text{ N}. \quad (28)$$

With $\xi = 1 \times 10^{-7}$, then, the nondimensionalized constants in (10) are

$$\bar{a} = -4.2, \quad \bar{b} = -640, \quad \bar{c} = 350. \quad (29)$$

For the numerical experiments below, we let the surface tension, $\bar{\tau}$, vary from 1 to 100 and the surface anchoring, $\bar{\varpi}$ vary from 0.01 to 1. This corresponds to a dimensionalized surface tension, σ , ranging from $10^{-4} - 10^{-2} \text{ N}$ and anchoring values ranging from $10^{-6} - 10^{-2} \text{ N}$. Moreover, we artificially scale the Landau coefficients so that the defect size is ~ 10 its true value. The scalar order parameter S_0 for the tangential anchoring is initialized as

$$S_0 = \frac{-\bar{b} + \sqrt{\bar{b}^2 - 24\bar{a}\bar{c}}}{4\bar{c}} = 0.933567.$$

For the rest of the section, we assume all quantities are suitably nondimensionalized and drop the bar notation.

For all test problems, the initial guess is defined on a circle of area 1 with equally distributed vertices representing the degrees of freedom, $\mathbf{x} \in M$. Here, $|M_i|$ denotes the number of vertices on grid M_i . The initial director field is aligned parallel to the x -axis. We solve the problems on various grids of different sizes: $|M_1| = 16$, $|M_2| = 49$, $|M_3| = 169$, $|M_4| = 625$, $|M_5| = 2401$, $|M_6| = 9409$. With NI, we start on grid M_1 and end at grid M_6 . NI results are compared with results on the single finest grid, M_6 . We assess this initial guess' feasibility based on the extent of deformation required to reach the final configuration, considering both orientational order and spatial location adjustments. Strong tangential anchoring implies a significant orientation deformation, as directors must cover a substantial angular distance from their initial horizontal orientation. Similarly, sizable spatial deformation arises from increased anisotropic surface tension due to the considerable distance between the initial spherical state and highly elongated configurations.

4.1. Physical Validation

Before modeling the dynamics of the full (\mathbf{x}, Q) optimization, we aim to understand the separate role of shape and order degrees of freedom by defining two subproblems derived from (12):

Subproblem A.

$$Q^* = \arg \min_Q F(\mathbf{x}^*, Q). \quad (30)$$

Subproblem B.

$$\begin{aligned} M^* &= \arg \min_{\mathbf{x} \in M} F(\mathbf{x}, Q^*), \\ s.t. \quad &0 = C(\mathbf{x}). \end{aligned} \tag{31}$$

In Subproblem A, (30), we assume the grid, M^* , with vertices \mathbf{x}^* is fixed and at equilibrium. Similarly, for Subproblem B, (31), the field, or Q-tensor, is at equilibrium, Q^* defined on M .

Solutions to Subproblem A, (30), are director fields with different alignments strongly affected by the isotropic surface tension τ while the anchoring parameter remains small at $\omega = 0.2$. The surface terms from (30) can be split into two parts: the line tension integral,

$$\tau \int_{\partial M} ds, \tag{32}$$

and the surface anchoring integral,

$$\frac{\tau\omega}{2} \int_{\partial M} \text{tr} (Q - Q_s)^2 ds. \tag{33}$$

With the grid fixed, as we increase τ , we only see an effect from the surface anchoring integral as it depends on the Q-tensor. Here, the prefactor $\Gamma = \frac{\tau\omega}{2}$ promotes stronger tangential anchoring as τ increases. Following Bates' conclusion [13], we expect to see stronger tangential alignment on the domain's boundary as τ increases as well as the emergence of two defects [4, 5] that become physicalized in the domain. This is confirmed in Figures 1 and 2.

We compare the results of QN with and without nested iteration for various values of τ on grids up to M_6 . We retain the overall shape of the domain, a dodecagon, from the coarsest grid. The left graphics of Figures 1 and 2 show the distribution of the scalar order parameter S , and the corresponding director field is given on the right. Both QN and QN with NI depict two defects appearing with stronger surface anchoring, as expected. Both methods also demonstrate that the director field anchors to the boundary as τ tends to 100. We note that the solution from nested iteration locates the defect pair near two opposing vertices of the polygonal boundary, but as shown in Table 1, the two methods have converged to similar energies.

Table 1 depicts the number of Newton iterations for both QN on grid M_6 and QN with NI on each level of refinement. Note that for small values of τ , the equilibrium solution has already been found on grid M_5 , and no extra iterations are needed on grid M_6 as the nonlinear residuals are already quite small. The table also shows the converged energy, F^k , and the runtime in seconds for the simulations. We see that both QN alone and with NI yield the same converged solutions that minimize the energy. However, NI significantly improves the timing compared to QN alone by a factor of 37 to 71 times.

Conversely, solutions to Subproblem B, (31), are the various shapes that result at a fixed $\tau = 10$, but varying ω . With the molecular alignment fixed across the shape, we see an effect from both line tension (32) and anchoring (33) integrals, as Γ now indicates stronger *anisotropic* surface tension on the spatial coordinates of the nematic LC molecules. The increasing elongation of the shape illustrates this. As Prinsen and van

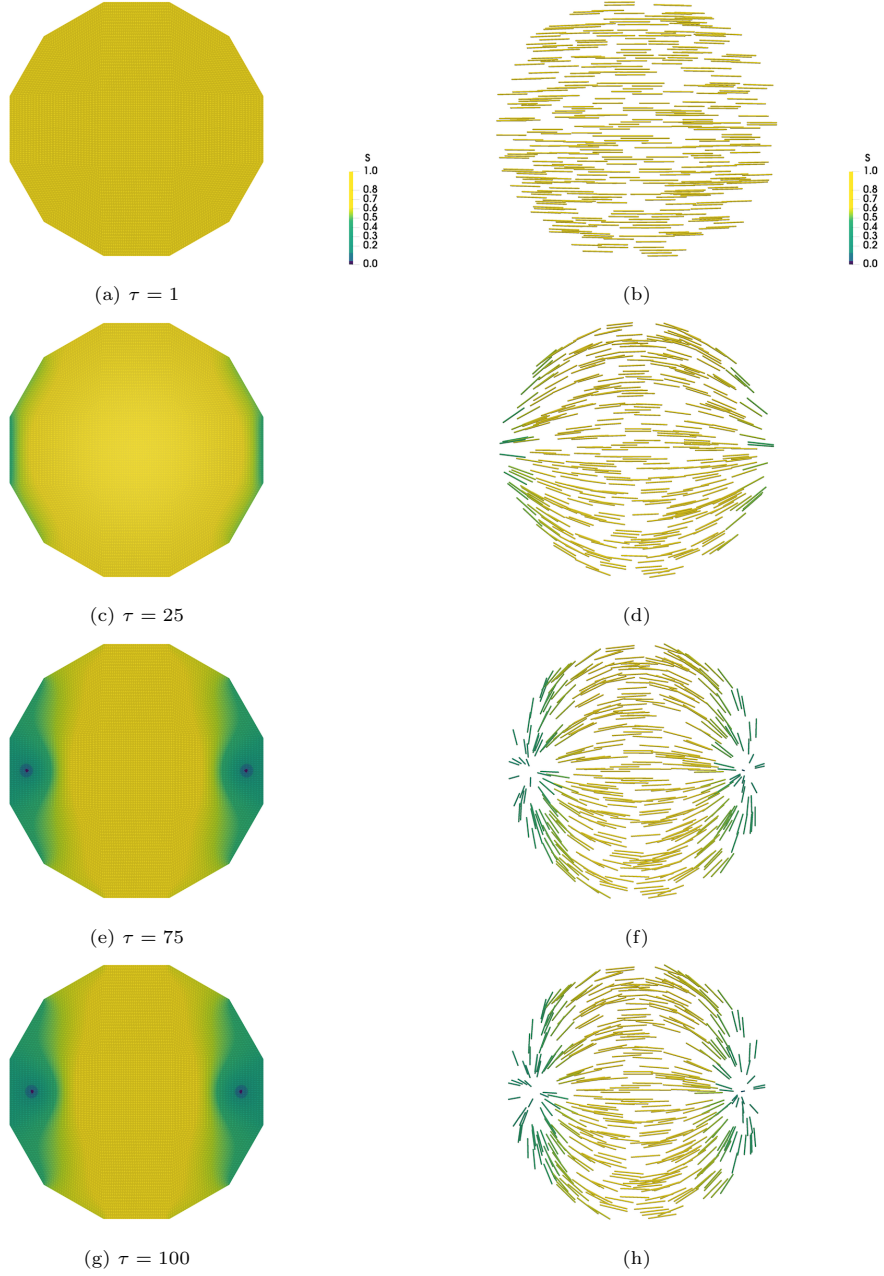


Figure 1: Applying QN for Subproblem A on M_6 . The color bar indicates the value of S , i.e., the order of the director field in the domain. Left plots, (a), (c), (e), (g), depict the order's distribution, illustrating two defects for higher τ . Right plots, (b), (d), (f), (h), show the directors' anchoring to the boundary as $\tau \rightarrow 100$ and also demonstrate the disorder around the defects.

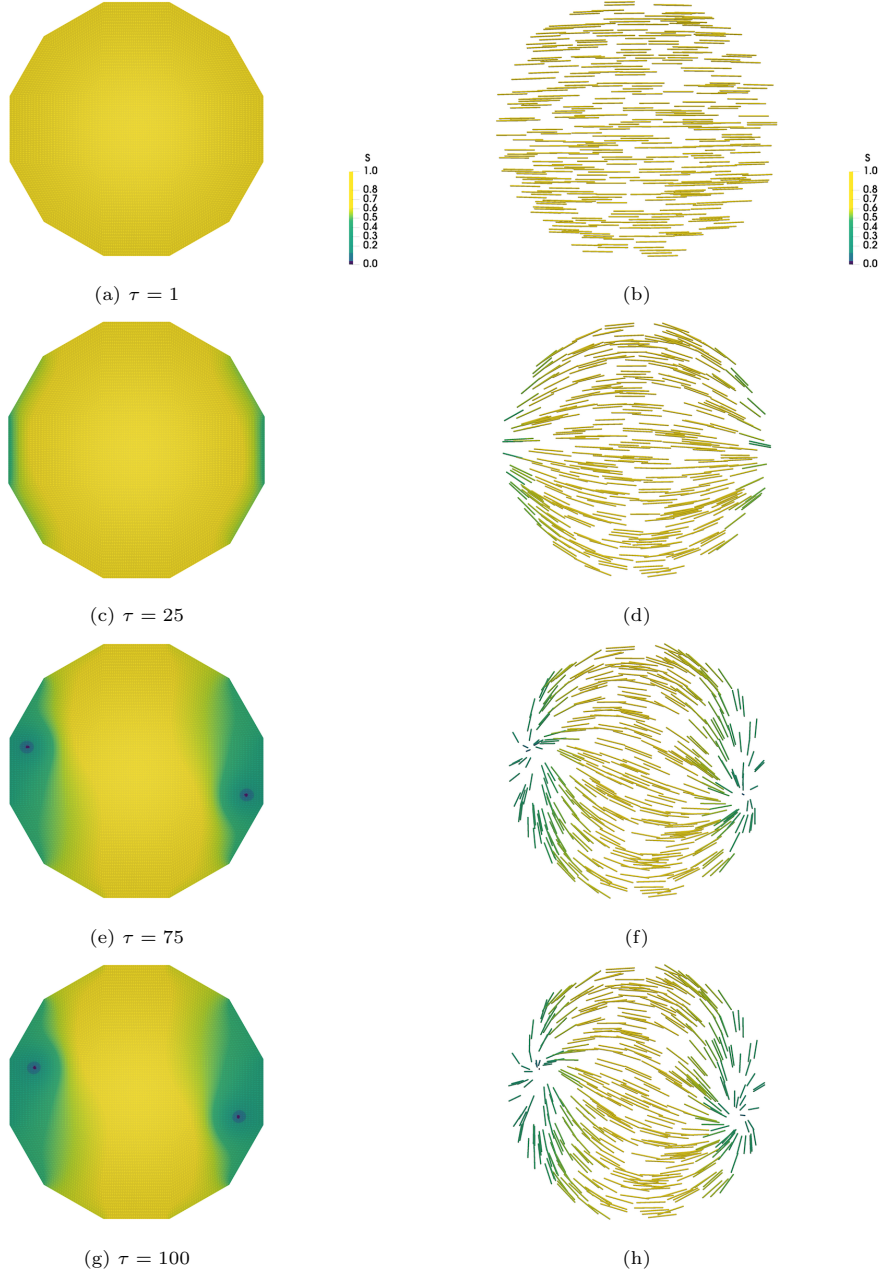


Figure 2: Applying QN with NI for Subproblem A. Results shown on grid M_6 . The color bar indicates the value of S , i.e., the order of the director field in the domain. Left plots, (a), (c), (e), (g), depict the order's distribution illustrating two defects for higher τ . Right plots, (b), (d), (f), (h), show the directors' anchoring to the boundary as $\tau \rightarrow 100$ and also demonstrate the disorder around the defects.

	$\tau = 1$	25	75	100
NI Grid	Iterations			
M_1	26	34	39	41
M_2	15	39	70	59
M_3	7	25	53	50
M_4	8	17	69	26
M_5	1	7	11	11
M_6	0 (75)	0 (102)	1 (152)	1 (148)
F^k	-19.88 (-19.88)	-15.04 (-15.04)	-12.31 (-12.31)	-12.02 (-12.02)
Runtime [sec]	16.05 (1, 151.91)	28.43 (1, 566.53)	62.59 (2, 336.07)	54.24 (2, 260.82)

Table 1: Subproblem A: Iteration count for QN with NI on each grid level. Iteration count for QN without NI is given on level M_6 in parenthesis. The final energy, F^k , and runtime in seconds for the full simulation of QN with NI (QN without NI in parenthesis) are also given. Both QN and QN with NI converge to the same energies for all τ . NI improves efficiency in terms of iteration and runtime by taking minimal, if any, steps on the finest grid.

der Schoot [2] showed, the tactoid morphology depends on the balance of surface and bulk forces and on the ratio of the anisotropic to isotropic surface tension, $\frac{\Gamma}{\tau}$. With the molecular alignment fixed, their results illustrate that for $\omega \ll 1$, the aspect ratio is expected to scale $1 + \omega$. Even though we fix $\tau = 10$ and bulk constants, a, b, c in Subproblem B, we mimic their results numerically by increasing ω from 0.01 to 1 indicating that the shape’s aspect ratio is ω -dependent.

We do not present standalone QN results as these did not converge for every value of ω . As the shape changes, the initial circular guess is further from the optimal configuration, causing the method to stagnate. As expected, NI improves the initial guesses on each successive grid level, providing convergent results. Thus, we only use QN with NI to perform physical validation. Figure 3 displays the hierarchy of adaptive grids used in the simulation for the extreme ends of shape change (i.e., $\omega = 0.01$ and $\omega = 1$). In Figure 4, we again show the distribution of the scalar order parameter S (left plots), and the corresponding director field (right plots). We see the aspect ratio of the shape increasing as ω increases, validating Prinsen and van der Schoot’s theory. Note that with the Q held constant, the order of the director field is fixed at $S_0 = 0.933567$, and each director is horizontal to the x -axis. We do not expect to see defects virtualizing, only the tactoid elongating as the anisotropic surface tension strength increases.

4.2. Full (\mathbf{x}, Q) Optimization

The previous subproblems allow us to understand the individual effect on the presence of defects with τ and on the shape’s trend of deformation driven by ω . Numerically, we demonstrated that nested iteration significantly improved timings for examples with high orientational deformations and a notable improvement in convergence for regions of high spatial deformations. In this section, we allow both spatial and orientational movements, with the intention of comparing QN, derived in Section 3.2, with the GD method in Section 3.1 and seeing the effect of NI on both approaches. In doing so, we validate the same results from Subproblems A and B while tracking the distribution of the scalar order parameter S , the corresponding director field, the converged energy F^k , the

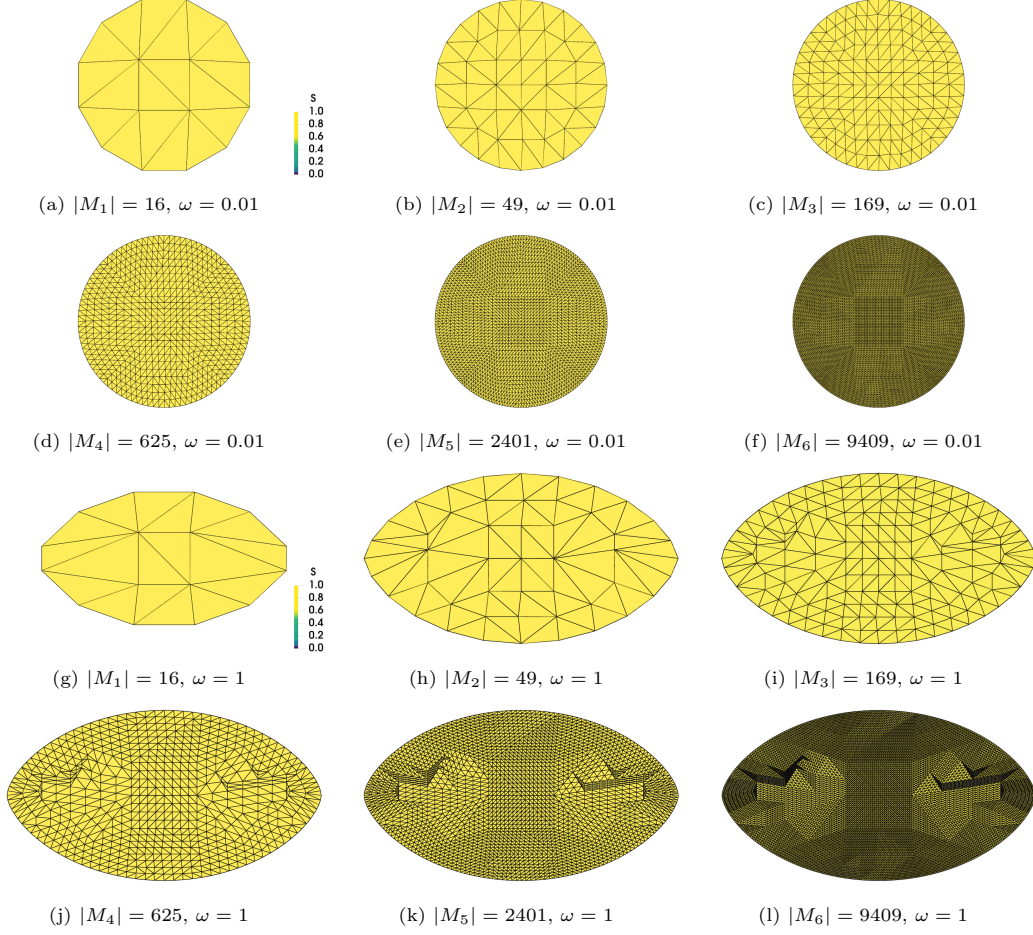


Figure 3: Applying QN with NI for Subproblem B: Grids for each NI level for $\omega = 0.01$ (top two rows) and $\omega = 1$ (bottom two rows).

number of iterations for each grid level, and the runtime in seconds. In these numerical experiments, we mimic Subproblem B by holding τ fixed at 10 and varying ω from 0.01 to 1. Since we allow for spatial and orientational displacements, we expect to see an effect from both isotropic surface tension (32) and anchoring effects (33). Visually, in this case, we expect to see the colloidal particles elongating and virtualizing two defects on the opposite ends of the shape as ω tends to 1. This is the combined effect of the dynamic interplay of the isotropic and anisotropic strengths on tactoids.

Similarly to the subproblems above, we show the NI grid progression on the levels for $\omega = 0.01$ and $\omega = 1$. Figure 5 illustrates the finite-element mesh evenly distributed throughout the grids in the absence of defects. For $\omega = 1$, the vertices of the mesh collect around the two defects as the grids get larger, indicating that the defects are virtualizing as the shape is elongated and the directors are collecting around the defect's region.

Next, Figure 6 exhibits the combined effects from shape change and orientational vari-

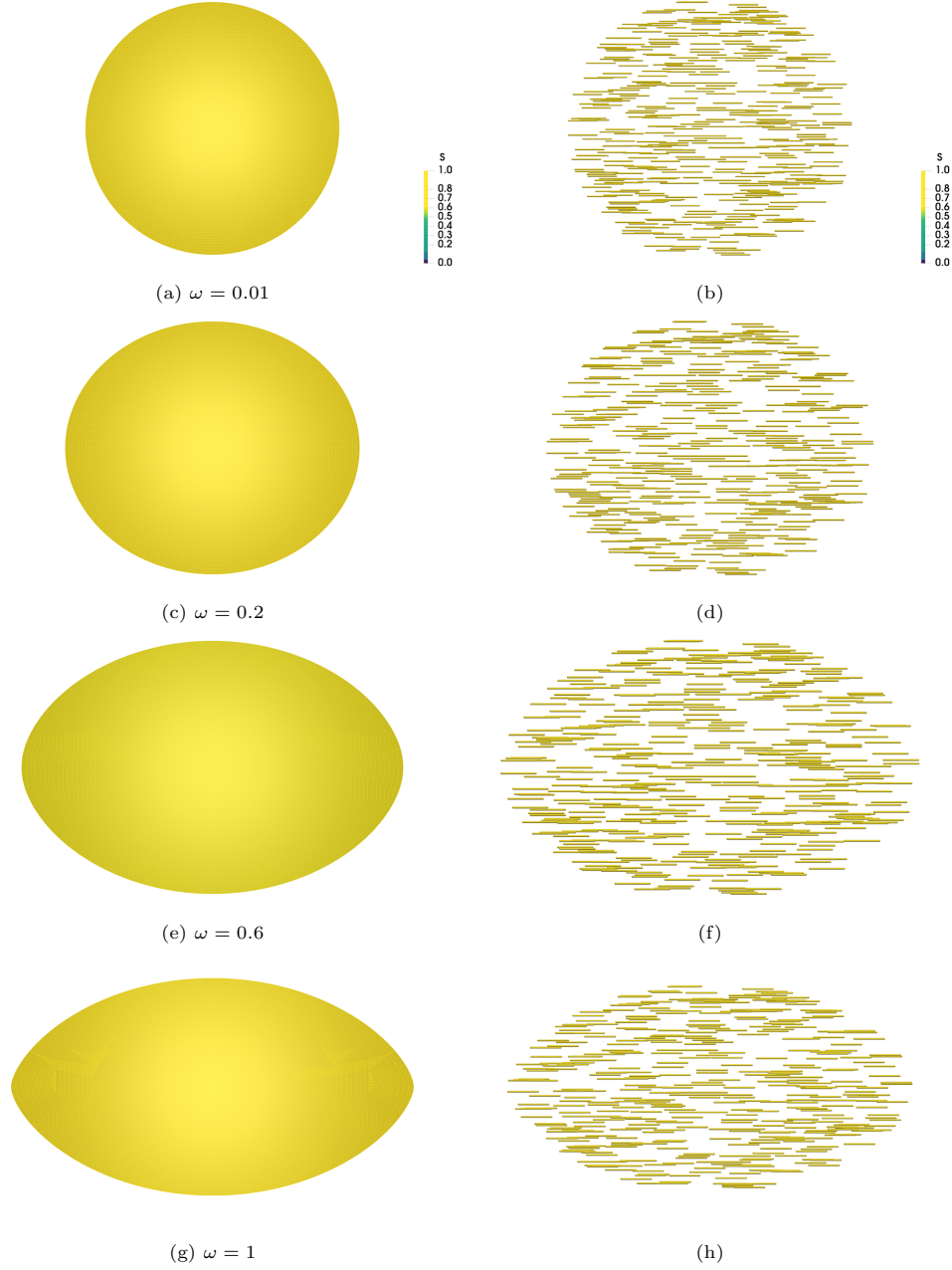


Figure 4: Applying QN with NI for Subproblem B. Results shown on grid M_6 . The color bar indicates the value of S , i.e., the order of the director field in the domain. Left plots, (a), (c), (e), (g), depict the order's distribution. Right plots, (b), (d), (f), (h), show the fixed horizontally-aligned directors. Dramatic shape change is shown as $\omega \rightarrow 1$.

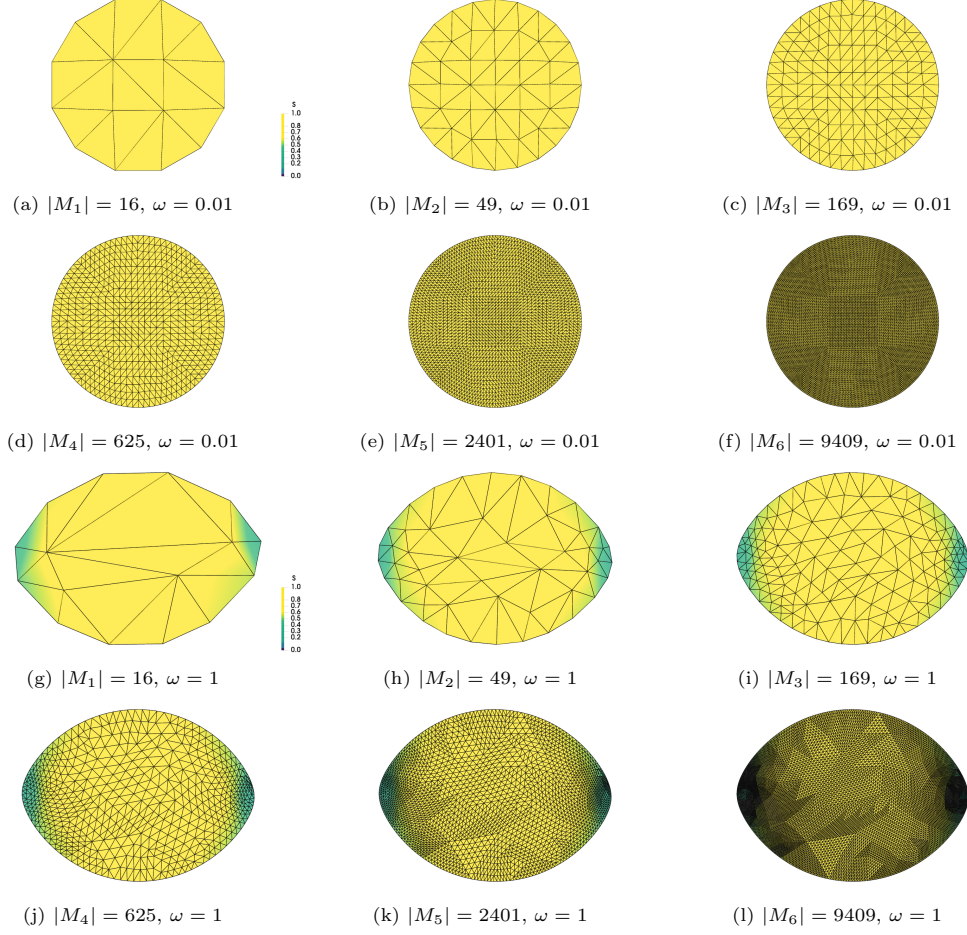


Figure 5: Applying QN with NI for full (\mathbf{x}, Q) problem: Grids for each NI level for $\omega = 0.01$ (top two rows) and $\omega = 1$ (bottom two rows).

ance as ω tends to 1 using QN with NI. As expected, we see non-spherical shapes with increasing anisotropic surface tension. Consequently, we see the director field anchoring to the boundary as the prefactor Γ increases in the anchoring integral (33). Mimicking results in [13], defects appear as the shape elongates. As discussed for Subproblem A, we note that nested iteration does find rotationally invariant solutions. Finally, corroborating results found in [2] and [48], Figure 7 shows the relationship between aspect ratio of the shape to anchoring strength, ω . We see a strong logarithmic trend in aspect ratio in the presence of changing molecular alignment (full problem) in contrast to a linear trend for fixed alignment (Subproblem B) as predicting by the scaling analysis done in [2].

To compare the performance of GD and QN with and without NI, iteration counts, final energy, and runtimes are included in Table 2. NI yields significant improvement for both GD and QN. We note that sensitivity to spatial deformation depends on grid size, as GD did not converge on any M_6 grid across all the values ω . Similarly, QN without

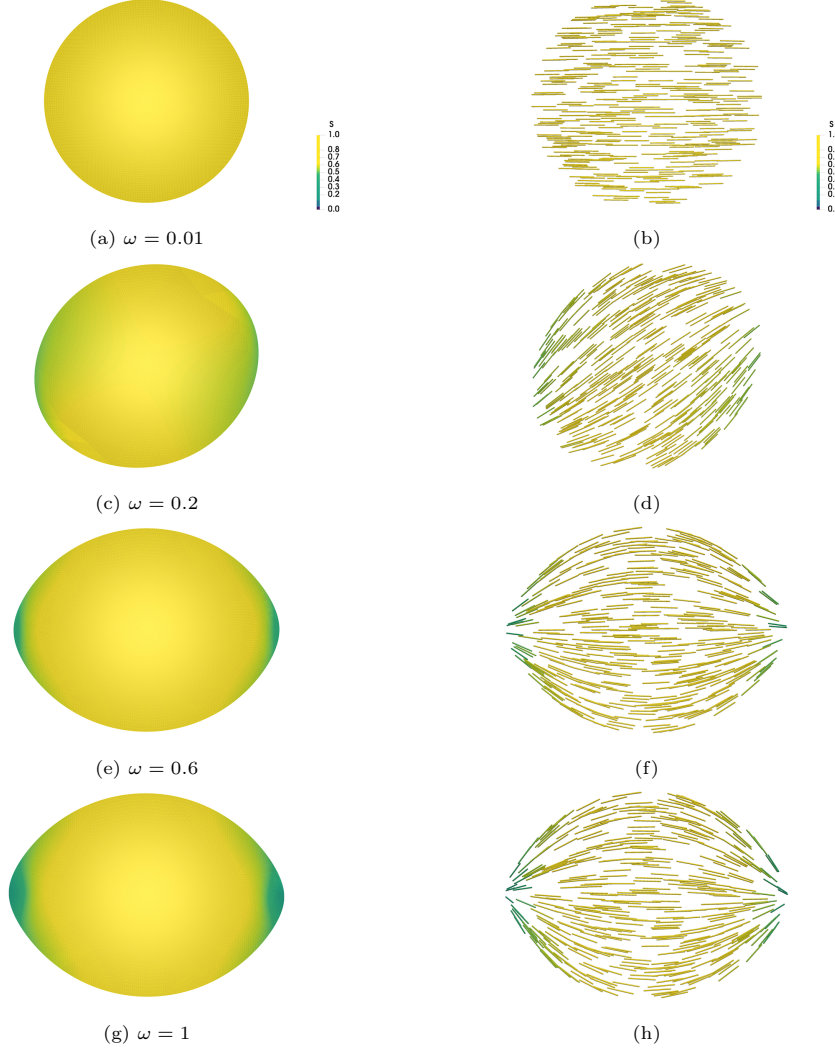


Figure 6: Applying QN with NI to full (\mathbf{x}, Q) problem. Results shown on grid M_6 . The color bar indicates the value of S , i.e., the order of the director field in the domain. Left plots, (a), (c), (e), (g), depict the order's distribution. Right plots, (b), (d), (f), (h), show the directors with stronger anchoring as the shape changes with $\omega \rightarrow 1$. Areas in green indicate less order, showing the appearance of the defects, as expected.

NI failed for large ω , and found nearby local solutions for small values on grid M_6 , but at a large increase in computational time. With nested iteration, the iteration counts for the full shape optimization problem dramatically decrease as we refine the grid. While GD still requires several hundred iterations for large ω , QN with NI converged in only a couple of iterations on the finest grid. This improved performance is further illustrated in Figure 8 showcasing that the average runtime for QN with NI for the full problem is consistently lower than GD with NI as $\omega \rightarrow 1$.

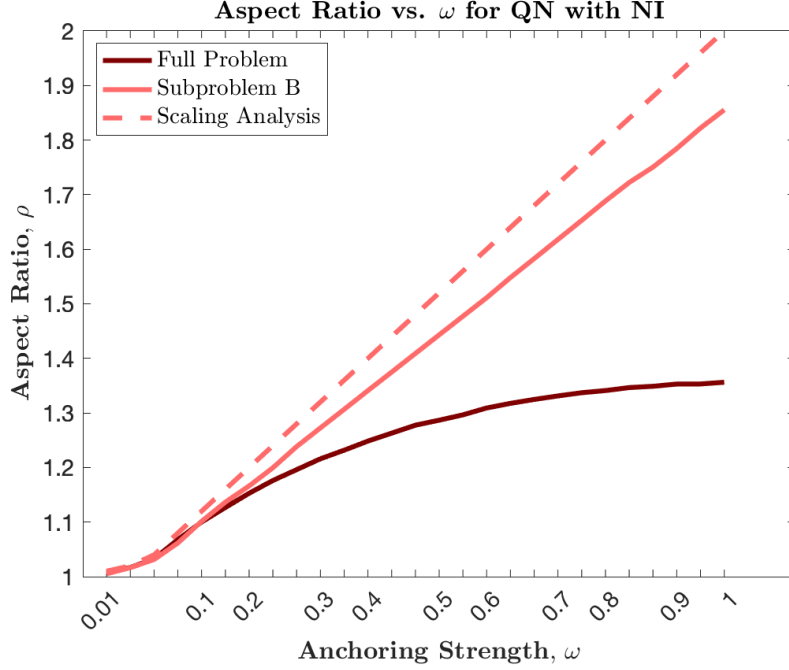


Figure 7: Applying QN with NI to full (\mathbf{x}, Q) problem and Subproblem B: With the presence of molecular alignment (dark red) for the full problem, we see a logarithmic effect in aspect ratio compared to the linear trend (light red) for fixed alignment in Subproblem B. For fixed alignment, this is in agreement with the scaling analysis done in [2] (dashed line).

5. Discussion and Future Work

The present work describes an “all in one” quasi-Newton approach to modeling a challenging class of nematic liquid crystal tactoid shape optimization problems, where the equilibrium configuration of the model must be found by minimizing a free energy functional with respect to the orientational order and shape of the domain. This approach is effective for this class of problems as it does not require maintenance of mesh quality during the minimization process, has an accurate line search procedure that dynamically updates all unknown variables simultaneously, and allows one to efficiently simulate the solutions on a large scale by uniformly increasing the resolution via nested iteration.

Exploring the space of shapes as a function of surface tension and anisotropic elastic constants, we find the nematic tactoids forming under conditions similar to those observed elsewhere [2, 13]. Our main goal here was to improve existing numerical algorithms used to find the equilibrium configurations while ensuring physical validity. We found that through the use of nested iteration, where we gradually refine the initial guess towards a solution with high resolution, we are able to preserve accuracy and robustness with low computational costs.

Future work involves solving the linearized steps iteratively using multigrid methods to reduce the computational cost further while maintaining the same level of accuracy and efficiency. In addition, we plan to apply the methods discussed in this work to other

GD with NI	$\omega = 0.01$	0.2	0.4	0.6	0.8	1
NI Grid	Iterations					
M_1	1000	28,500	22,300	8,300	7,100	7,100
M_2	250	14,400	21,600	20,600	18,600	1,800
M_3	190	3,00	5,600	5,200	6,100	6,900
M_4	130	550	1,200	1,600	1,900	2,100
M_5	38	415	700	800	800	900
M_6	4 (–)	250 (–)	600 (–)	600 (–)	600 (–)	600 (–)
F^k	15.41 (–)	17.70 (–)	19.17 (–)	20.10 (–)	20.72 (–)	21.13 (–)
Runtime [sec]	16.21 (–)	390.32 (–)	478.27 (–)	429.27 (–)	466.85 (–)	507.58 (–)
QN with NI	$\omega = 0.01$	0.2	0.4	0.6	0.8	1
NI Grid	Iterations					
M_1	35	187	155	95	108	113
M_2	11	106	180	184	181	207
M_3	5	23	89	106	123	146
M_4	5	12	16	24	23	26
M_5	3	7	9	9	11	8
M_6	2 (56)	2 (120)	4 (–)	5 (–)	2 (–)	2 (–)
F^k	15.41 (14.25)	17.70 (17.63)	19.17 (–)	20.10 (–)	20.72 (–)	21.13 (–)
Runtime [sec]	127.08 (2,775.90)	163.31 (6,104.24)	283.78 (–)	340.15 (–)	198.76 (–)	195.26 (–)

Table 2: Full (\mathbf{x}, Q) problem. Iteration count for GD with NI (top) and QN with NI (bottom) on each grid level. Iteration count for methods without NI is given on level M_6 in parenthesis. The final energy, F^k , and runtime in seconds for the full simulation with NI and without in parenthesis are also given. Standalone QN for small ω converges to a local minimum at the cost of long runtime, whereas standalone GD does not converge for any ω on M_6 (indicated by –). NI improves efficiency for both methods in terms of iteration and runtime.

Q-tensor models and compare them against experimental results. Finally, including the study of inequality constraints that simulate the formation of nematic tactoids in bounded channels will be considered.

Acknowledgments

This work was supported by the National Science Foundation under Grant No. ACI-2003820. The authors of this paper would like to thank Dr. Xiaozhe Hu, Dr. Chaitanya Joshi, and Dr. Viviana Betancur for their valuable discussions.

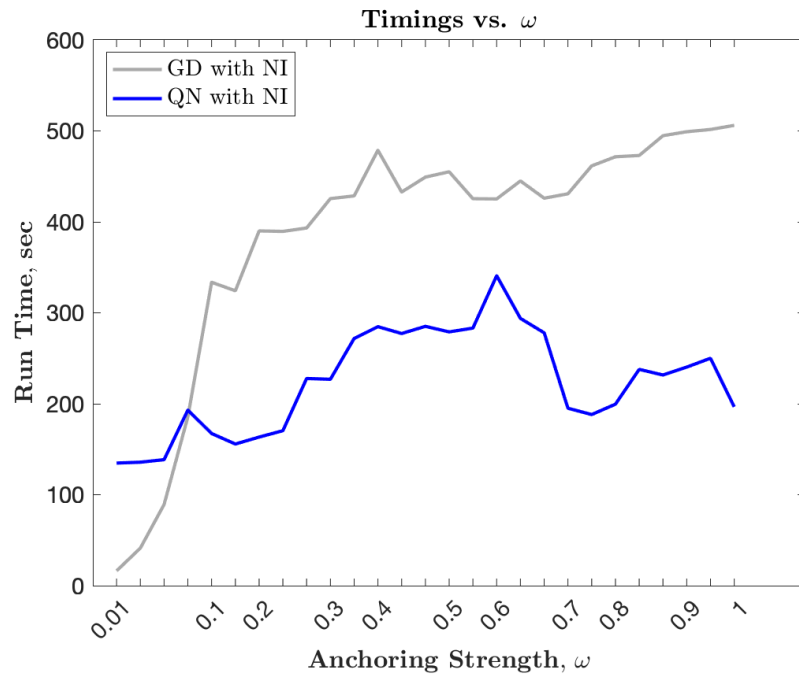


Figure 8: For the full (\mathbf{x}, Q) problem, QN with NI uses less computational resources on *average* than GD with NI as $\omega \rightarrow 1$.

References

- [1] P.-G. D. Gennes, J. Prost, The physics of liquid crystals, Oxford university press, 1993.
- [2] P. Prinsen, P. V. D. Schoot, Shape and director-field transformation of tactoids, *Physical Review E* 68 (2003) 1–11. doi:<https://doi.org/10.1103/PhysRevE.68.021701>.
- [3] S. Chandrasekhar, Surface tension of liquid crystals, *Molecular Crystals and Liquid Crystals* 2 (1966) 71–80. doi:<https://doi.org/10.1080/15421406608083061>.
- [4] J. Dzubiella, M. Schmidt, H. Löwen, Topological defects in nematic droplets of hard spherocylinders, *Physical Review E* 62 (2000) 5081–5091.
- [5] C. E. Sitta, F. Smallenburg, R. Wittkowski, H. Löwen, Liquid crystals of hard rectangles on flat and cylindrical manifolds, *Physical Chemistry Chemical Physics* 20 (2018) 5285–5294. doi:<https://doi.org/10.1039/C7CP07026H>.
- [6] J. P. F. Lagerwall, G. Scalia, A new era for liquid crystal research: Applications of liquid crystals in soft matter nano-, bio-and microtechnology, *Current Applied Physics* 12 (2012) 1387–1412. doi:<https://doi.org/10.1016/j.cap.2012.03.019>.
- [7] P. der Asdonk, P. H. J. Kouwer, Liquid crystal templating as an approach to spatially and temporally organise soft matter, *Chemical Society Reviews* 46 (2017) 5935–5949. doi:<https://doi.org/10.1039/C7CS00029D>.
- [8] S. T. Stealey, A. K. Gaharwar, S. P. Zusiak, Laponite-based nanocomposite hydrogels for drug delivery applications, *Pharmaceuticals* 16 (2023) 1–19. doi:[10.3390/ph16060821](https://doi.org/10.3390/ph16060821).
- [9] R. Mascarenhas, G. Kaur, Electrically conductive polymer-clay nanocomposites, Vol. 2535, 2023, pp. 1–15. doi:<https://doi.org/10.1063/5.0115418>.
- [10] M. Wehner, R. L. Truby, D. J. Fitzgerald, B. Mosadegh, G. M. Whitesides, J. A. Lewis, R. J. Wood, An integrated design and fabrication strategy for entirely soft, autonomous robots, *nature* 536 (2016) 451–455. doi:[10.1038/nature19100](https://doi.org/10.1038/nature19100).
- [11] D. S. Shah, J. P. Powers, L. G. Tilton, S. Kriegman, J. Bongard, R. Kramer-Bottiglio, A soft robot that adapts to environments through shape change, *Nature Machine Intelligence* 3 (2021) 51–59. doi:<https://doi.org/10.1038/s42256-020-00263-1>.
- [12] F. J. Schwarzendahl, P. Ronceray, K. L. Weirich, K. Dasbiswas, Self-organization and shape change by active polarization in nematic droplets, *Physical Review Research* 3 (2021) 1–6. doi:<https://doi.org/10.1103/PhysRevResearch.3.043061>.
- [13] M. A. Bates, G. Skačej, C. Zannoni, Defects and ordering in nematic coatings on uniaxial and biaxial colloids, *Soft Matter* 6 (2010) 655–663. doi:<https://doi.org/10.1039/B917180K>.
- [14] M. A. Bates, Computer simulation studies of nematic liquid crystal tactoids, *Chemical physics letters* 368 (2003) 87–93. doi:[https://doi.org/10.1016/S0009-2614\(02\)01824-9](https://doi.org/10.1016/S0009-2614(02)01824-9).
- [15] X. Xing, H. Shin, M. J. Bowick, Z. Yao, L. Jia, M.-H. Li, Morphology of nematic and smectic vesicles, *Proceedings of the National Academy of Sciences* 109 (2012) 5202–5206. doi:[10.1073/pnas.1115684109](https://doi.org/10.1073/pnas.1115684109).
- [16] L. Ding, R. A. Pelcovits, T. R. Powers, Deformation and orientational order of chiral membranes with free edges, *Soft Matter* 17 (2021) 6580–6588. doi:<https://doi.org/10.1039/D1SM00629K>.
- [17] N. B. Ludwig, K. L. Weirich, E. Alster, T. A. Witten, M. L. Gardel, K. Dasbiswas, S. Vaikuntanathan, Nucleation and shape dynamics of model nematic tactoids around adhesive colloids, *The Journal of chemical physics* 152 (2020) 1–12. doi:<https://doi.org/10.1063/1.5141997>.
- [18] L.-Q. Chen, Phase-field models for microstructure evolution, *Annual review of materials research* 32 (2002) 113–140. doi:[10.1146/annurev.matsci.32.112001.132041](https://doi.org/10.1146/annurev.matsci.32.112001.132041).
- [19] P. Cermelli, A. J. D. Scala, Constant-angle surfaces in liquid crystals, *Philosophical Magazine* 87 (2007) 1871–1888. doi:<https://doi.org/10.1080/14786430601110364>.
- [20] F. Gibou, R. Fedkiw, S. Osher, A review of level-set methods and some recent applications, *Journal of Computational Physics* 353 (2018) 82–109. doi:<https://doi.org/10.1016/j.jcp.2017.10.006>.
- [21] I. Nitschke, S. Reuther, A. Voigt, Liquid crystals on deformable surfaces, *Proceedings of the Royal Society A* 476 (2020) 1–23. doi:<https://doi.org/10.1098/rspa.2020.0313>.
- [22] C. D. Schimming, J. Viñals, S. W. Walker, Numerical method for the equilibrium configurations of a maier-saupe bulk potential in a q-tensor model of an anisotropic nematic liquid crystal, *Journal of Computational Physics* 441 (2021) 1–21. doi:<https://doi.org/10.1016/j.jcp.2021.110441>.
- [23] A. DeBenedictis, T. J. Atherton, Shape minimisation problems in liquid crystals, *Liquid Crystals* 43 (2016) 2352–2362. doi:<https://doi.org/10.1080/02678292.2016.1209699>.
- [24] J. H. Adler, T. J. Atherton, D. B. Emerson, S. P. MacLachlan, An energy-minimization finite-element approach for the frank-osen model of nematic liquid crystals, *SIAM Journal on Numerical Analysis* 53 (2015) 2226–2254. doi:<https://doi.org/10.1137/140956567>.

- [25] J. Nocedal, S. J. Wright, Numerical optimization, Springer, 1999.
- [26] C. G. Broyden, J. E. D. Jr, J. J. Moré, On the local and superlinear convergence of quasi-newton methods, IMA Journal of Applied Mathematics 12 (1973) 223–245. doi:<https://doi.org/10.1093/imamat/12.3.223>.
- [27] G. Starke, Gauss–newton multilevel methods for least-squares finite element computations of variably saturated subsurface flow, Computing 64 (2000) 323–338. doi:[10.1007/s006070070028](https://doi.org/10.1007/s006070070028).
- [28] W. L. Briggs, V. E. Henson, S. F. McCormick, A multigrid tutorial, SIAM, 2000.
- [29] U. Trottenberg, C. W. Oosterlee, A. Schuller, Multigrid, Elsevier, 2000.
- [30] J. H. Adler, D. B. Emerson, S. P. MacLachlan, T. A. Manteuffel, Constrained optimization for liquid crystal equilibria, SIAM Journal on Scientific Computing 38 (2016) B50–B76. doi:<https://doi.org/10.1137/141001846>.
- [31] P. E. Farrell, A. Birkisson, S. W. Funke, Deflation techniques for finding distinct solutions of nonlinear partial differential equations, SIAM Journal on Scientific Computing 37 (2015) A2026–A2045. doi:<https://doi.org/10.1137/140984798>.
- [32] J. H. Adler, D. B. Emerson, P. E. Farrell, S. P. MacLachlan, Combining deflation and nested iteration for computing multiple solutions of nonlinear variational problems, SIAM Journal on Scientific Computing 39 (2017) B29–B52. doi:<https://doi.org/10.1137/16M1058728>.
- [33] D. B. Emerson, P. E. Farrell, J. H. Adler, S. P. MacLachlan, T. J. Atherton, Computing equilibrium states of cholesteric liquid crystals in elliptical channels with deflation algorithms, Liquid Crystals 45 (2018) 341–350. doi:<https://doi.org/10.1080/02678292.2017.1365385>.
- [34] J. Xia, S. MacLachlan, T. J. Atherton, P. E. Farrell, Structural landscapes in geometrically frustrated smectics, Physical Review Letters 126 (2021) 1–6. doi:[10.1103/PhysRevLett.126.177801](https://doi.org/10.1103/PhysRevLett.126.177801).
- [35] A. Ramage, E. C. G. Jr, A preconditioned nullspace method for liquid crystal director modeling, SIAM Journal on Scientific Computing 35 (2013) B226–B247. doi:<https://doi.org/10.1137/120870219>.
- [36] R. H. Nochetto, S. W. Walker, W. Zhang, A finite element method for nematic liquid crystals with variable degree of orientation, SIAM Journal on Numerical Analysis 55 (2017) 1357–1386. doi:<https://doi.org/10.1137/15M103844X>.
- [37] C. S. MacDonald, J. A. Mackenzie, A. Ramage, A moving mesh method for modelling defects in nematic liquid crystals, Journal of Computational Physics: X 8 (2020) 1–18. doi:<https://doi.org/10.1016/j.jcp.2020.100065>.
- [38] J. Xia, P. E. Farrell, Variational and numerical analysis of a q-tensor model for smectic-a liquid crystals, ESAIM: Mathematical Modelling and Numerical Analysis 57 (2023) 693–716. doi:<https://doi.org/10.48550/arXiv.2110.06479>.
- [39] F. C. Frank, I. liquid crystals. on the theory of liquid crystals, Discussions of the Faraday Society 25 (1958) 19–28. doi:<https://doi.org/10.1039/DF9582500019>.
- [40] N. J. Mottram, C. J. P. Newton, Introduction to q-tensor theory, arXiv preprint arXiv:1409.3542 (2014) 1–20. doi:<https://doi.org/10.48550/arXiv.1409.3542>.
- [41] M. Nestler, I. Nitschke, A. Voigt, A finite element approach for vector-and tensor-valued surface pdes, Journal of Computational Physics 389 (2019) 48–61. doi:<https://doi.org/10.1016/j.jcp.2019.03.006>.
- [42] P. E. Farrell, A. Hamdan, S. P. MacLachlan, Finite-element discretization of the smectic density equation, IMA Journal of Numerical Analysis 00 (2023) 1–36. doi:<https://doi.org/10.48550/arXiv.2207.12916>.
- [43] A. E. Diegel, S. W. Walker, A finite element method for a phase field model of nematic liquid crystal droplets, Commun. Comput. Phys. 25 (2019) 155–188. doi:[10.4208/cicp.0A-2017-0166](https://doi.org/10.4208/cicp.0A-2017-0166).
- [44] J. P. Borthagaray, R. H. Nochetto, S. W. Walker, A structure-preserving fem for the uniaxially constrained q-tensor model of nematic liquid crystals, Numerische Mathematik 145 (2020) 837–881. doi:<https://doi.org/10.1007/s00211-020-01133-z>.
- [45] M. Hirsch, F. Weber, A convergent finite element scheme for the q-tensor model of liquid crystals subjected to an electric field, arXiv preprint arXiv:2307.11229 (2023). doi:<https://doi.org/10.48550/arXiv.2307.11229>.
- [46] M. Benzi, G. H. Golub, J. Liesen, Numerical solution of saddle point problems, Acta numerica 14 (2005) 1–137. doi:<https://doi.org/10.1017/S0962492904000212>.
- [47] F. Bach, R. Jenatton, J. Mairal, G. Obozinski, et al., Convex optimization with sparsity-inducing norms, Optimization for machine learning 5 (2011) 19–53.
- [48] C. Joshi, D. Goldstein, C. Wennerholm, E. Downey, E. Hamilton, S. Hocking, A. Andrei, J. H. Adler, T. J. Atherton, Morpho—a programmable environment for shape optimization and shapeshifting problems, arXiv preprint arXiv:2208.07859 (2022). doi:<https://doi.org/10.48550/arXiv.2208.07859>.

07859.